

Ni/Au contacts to corundum α -Ga₂O₃

F. Massabuau^{1*}, F. Adams², D. Nicol¹, J. Jarman², M. Frentrup², J. Roberts³, T.J. O'Hanlon⁴, A. Kovács⁵, P. Chalker³, and R. Oliver²

¹*Department of Physics, University of Strathclyde, Glasgow G4 0NG, UK*

²*Department of Material Science and Metallurgy, University of Cambridge, Cambridge CB3 0FS, UK*

³*School of Engineering, University of Liverpool, Liverpool L69 3GH, UK*

³*Plymouth Electron Microscopy Centre, University of Plymouth, Plymouth PL4 8AA, UK*

³*Ernst Ruska-Centre for Microscopy and Spectroscopy with Electrons, Forschungszentrum Jülich, 52425 Jülich, Germany*

E-mail: f.massabuau@strath.ac.uk

The structural, chemical and electrical properties of Ni/Au contacts to atomic layer deposited α -Ga₂O₃ were investigated. Ni forms a Schottky contact with α -Ga₂O₃, irrespectively of the post-annealing temperature. No sign of metal oxidation was observed at the metal-semiconductor interface (unlike what is observed for other metals like Ti), and instead, the metallurgical processes of the Ni-Au bilayer dominate the electrical properties. It is found that 400-450°C is the optimal annealing temperature, which allows for metal diffusion to heal gaps at the metal/semiconductor interface, but is not sufficient for Ni and Au to significantly interdiffuse and form an alloy with compositional inhomogeneities.

1. Introduction

Over the last decade, gallium oxide (Ga_2O_3) has emerged as a promising candidate for future wide bandgap optoelectronics, with applications entailing high-power electronics and solar-blind sensing¹⁻³). Ga_2O_3 is a highly polymorphic compound, with reported crystallographic phases labelled α , β , κ , γ and δ .⁴⁻⁶) The β -phase is the thermodynamically stable phase and has therefore received the most attention so far. In comparison, α - Ga_2O_3 is metastable but worthy of interest due to its wider bandgap and potential for bandgap engineering through alloying with other semiconducting sesquioxides.⁷⁻⁹) A consequence of that metastability is that progress with material synthesis has developed slower than for the β -phase, but nowadays strategies have been designed to reliably produce the metastable phases using most conventional deposition methods.¹⁰⁻¹¹)

Metal contacts are a central component of semiconductor devices, and the development of new semiconductor materials goes hand in hand with the development of the metal contacts that allow the new device to fulfil its purpose. For example, in the context of photodetectors, ohmic contacts often result in greater responsivity but slower response time, while Schottky contacts are associated with faster response time and lower dark current.¹²⁻¹³) Being the most studied polymorph, metal contacts to β - Ga_2O_3 have been investigated by several groups.¹⁴⁻¹⁸) These studies demonstrated that the conventional description of metal-semiconductor contacts borrowed from the Schottky-Mott model – which states that the rectifying or ohmic nature of the contact is determined by the work-function of the metal and the electron affinity of the semiconductor – falls short with Ga_2O_3 where many other factors have been found to play a non-negligible role. These include interfacial reaction between the oxide semiconductor and the metal,¹⁹⁻²¹) semiconductor orientation,¹⁸) morphology and thermal treatment.¹⁷) In comparison, metal contacts to the metastable phases have been overlooked, and the behaviour of contacts in these phases are often assumed to be identical to their β -phase equivalent. A phase-specific study of contacts is however necessary since many of the aforementioned factors – electron affinity, crystal orientation, chemical stability and morphology – are indeed, phase-dependent.

In a previous report, we investigated Ti/Au as a metal candidate for ohmic contact to α - Ga_2O_3 and highlighted that the electrical performance of the contact was the result of the competition between different processes including Ti oxidation by α - Ga_2O_3 with a mosaic structure, Ti-Au interdiffusion, and Au crystallization.²²) The different rates of each of these processes led to strong variations in contact performance with post-deposition treatment.

1
2
3 In the present study we turn our attention to Ni/Au as a candidate Schottky contact to α -
4 Ga_2O_3 . In β - Ga_2O_3 , Ni has been shown to form Schottky contacts^{13, 15, 18, 23, 24)} but the Fermi
5 level pinning and Schottky barrier height was shown to strongly depend on the crystal
6 orientation,^{15, 18, 23)} metal deposition method and thermal treatment.²⁴⁾ Already in β - Ga_2O_3 ,
7 little attention was paid to the other metallurgical and chemical mechanisms that arise in the
8 metal contact stack. As Ni contacts are often coated with Au, the interaction between these
9 two materials needs to be considered. Indeed, previous studies on GaN have demonstrated
10 that great amounts of diffusion between Ni and Au occurred at low annealing temperatures,
11 ²⁵⁻²⁷⁾ and even leading to dewetting at greater temperatures.²⁸⁾ In the present study we look
12 into the properties of Ni/Au contacts to α - Ga_2O_3 , and highlight the interplay between
13 metallurgical, chemical and electrical processes occurring within them.
14
15
16
17
18
19
20
21
22
23
24
25

26 2. Experimental methods

27 Films of non-intentionally n-doped α - Ga_2O_3 with thickness of *ca.* 250 nm were grown on *c*-
28 plane sapphire (α - Al_2O_3) substrates by plasma enhanced atomic layer deposition (PEALD)
29 using an Oxford Instruments OpAL reactor at a temperature of 250°C – a full description of
30 the growth process can be found in Ref. [29]. From previous investigations,²⁹⁻³⁰⁾ it is known
31 that under these growth conditions, the resulting α - Ga_2O_3 films grow epitaxially on the α -
32 Al_2O_3 substrate with $[0001]_{\text{Ga}_2\text{O}_3} \parallel [0001]_{\text{Al}_2\text{O}_3}$ and $[11\bar{2}0]_{\text{Ga}_2\text{O}_3} \parallel [11\bar{2}0]_{\text{Al}_2\text{O}_3}$. The films
33 consist dominantly of α - Ga_2O_3 columns, with amorphous and κ - Ga_2O_3 inclusions located
34 between the columns.³⁰⁾ The films were unintentionally n-doped, as was observed using X-
35 ray absorption spectroscopy and soft X-ray photoelectron spectroscopy by Swallow *et al.* on
36 comparable α - Ga_2O_3 films deposited by PEALD.³¹⁾
37
38
39
40
41
42
43
44
45

46 Following cleaning in acetone and isopropyl alcohol, metal contacts were defined using
47 ultraviolet lithography and thermal evaporation. Shipley s1813 positive photoresist was
48 developed with MF-319, an aqueous developer containing dilute tetramethylammonium
49 hydroxide (TMAH), after a short post-exposure treatment with chlorobenzene to produce
50 the undercut profile required for the metal lift-off process. After resist processing, 20 nm Ni
51 and 80 nm Au were evaporated by resistive thermal evaporation from tungsten boats, and
52 the patterns were lifted off in acetone. The contact structure consisted of circular pads 180
53 μm in diameter and spaced 500 μm apart. The samples were then annealed using rapid
54 thermal annealing for 2 minutes in N_2 ambient at temperatures ranging from 350°C to 600
55
56
57
58
59
60

1
2
3 °C, while one sample was kept un-annealed.

4
5 Atomic force microscopy (AFM) using a Bruker Dimension Icon Pro microscope operating
6 in peak force tapping mode was employed to record the topography of the α -Ga₂O₃ surface
7 before and after annealing.
8
9

10
11 X-ray diffraction (XRD) using a Philips X'pert MRD diffractometer consisting of a Cu K α
12 source, a four-bounce Ge crystal monochromator, and a three-bounce Ge crystal analyser
13 was employed to record the structure of the samples before and after annealing.
14
15

16
17 Photoelectric characterisation was performed using Keithley 6487 source-meter unit coupled
18 to a Signatone probe station. A Thorlabs SL S204 Deuterium light source coupled to a
19 SolarLS ML44 monochromator was used to excite the sample with a 240 nm light beam.
20
21
22

23
24 To observe the atomic and chemical structure of the samples, lamellae were prepared by
25 focussed ion beam (FIB) sputtering, and high-angle annular dark-field scanning transmission
26 electron microscopy (HAADF-STEM) imaging and energy-dispersive X-ray spectroscopy
27 (EDX) measurements were conducted using an aberration-corrected FEI Titan microscope³²⁾
28 operated at 200 kV and with ADF detector semi-angle of 69 mrad. EDX compositional maps
29 were obtained using the Cliff-Lorimer factor method.³³⁾
30
31
32
33

34 35 36 37 38 **3. Results and discussion**

39
40 Figure 1(a) shows XRD 2θ - ω scans for the as-deposited and annealed samples. Each
41 diffractogram exhibits an intense sharp peak at 41.7° corresponding to the 0006 reflection of
42 the α -Al₂O₃ substrate as well as a peak near 40.1-40.2° associated with the 0006 reflection
43 of the α -Ga₂O₃ film. Slight variations in α -Ga₂O₃ peak position are visible upon annealing,
44 in agreement with previous reports that annealing induces strain relaxation.^{22, 34)} Reflections
45 associated with the metal contact can also be observed. In the as-deposited structure, the 111
46 reflection of Au can be seen at 38.2°, while the 111 reflection of Ni at 44.8° is barely visible,
47 which is not unexpected given the thinness and potential low-crystallinity of the evaporated
48 Ni layer.
49
50
51
52
53
54
55
56
57
58
59
60

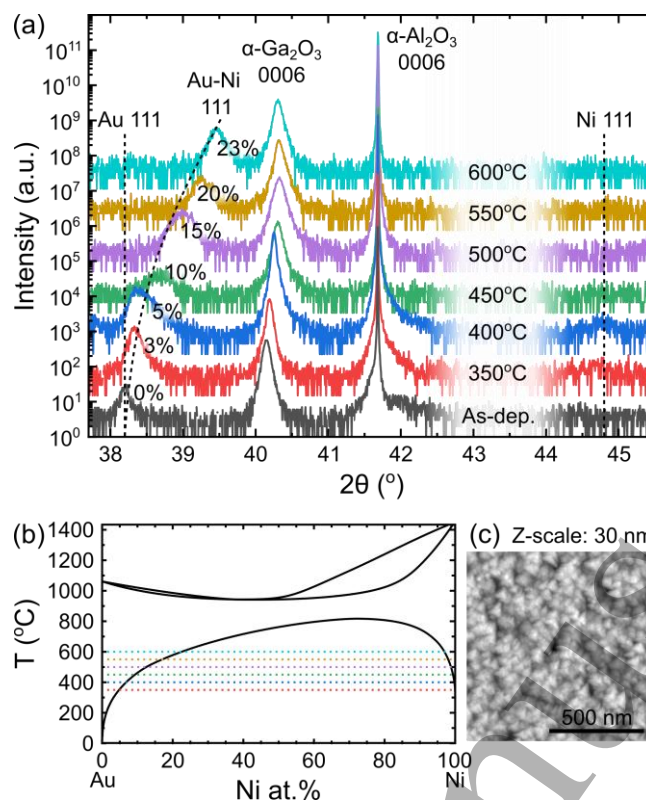


Fig. 1. (a) Symmetric 2θ - ω XRD scans of the samples annealed at different temperatures. (b) Redrawn phase diagram for Au-Ni. (c) AFM topography image of the $\alpha\text{-Ga}_2\text{O}_3$ surface.

For the structures that were annealed, we can see that the Au 111 peak (in the as-deposited sample) shifts substantially towards greater angles upon annealing at higher temperatures. This could be indicative of the formation of a Au-Ni alloy from the initial Ni-Au metal bilayer. Using the peak position to infer the lattice plane spacing and alloy composition assuming Vegard's law applies³⁵ we find that Au-Ni interdiffusion is limited at low annealing temperatures, with the Au-Ni alloy annealed at 400°C containing only 5% of Ni, but increases significantly for greater temperatures, reaching 23% of Ni for the Au-Ni alloy annealed at 600°C – see compositions labelled in Figure 1(a). Looking at the phase diagram for Au-Ni (Figure 1(b)), we can see that the alloy compositions obtained from XRD follow the expected miscibility of Ni in Au. It is perhaps surprising that a 2 min anneal is sufficient to reach an alloy composition close to that expected at thermodynamic equilibrium. We note that our results are aligned with previous reports from Herz *et al.* who studied a greater range of anneal conditions on Ni-Au bilayers and observed that this interdiffusion marked the early stages of the dewetting process.²⁸⁾

AFM was conducted to verify that the $\alpha\text{-Ga}_2\text{O}_3$ was not significantly affected by the annealing treatment. Indeed, we report no significant changes in topography, with the RMS roughness remaining within the 3.8-4.8 nm range across the whole sample set – in agreement

reviews (Oct. 2022)

with our previous observations.²²⁾ Figure 1(c) shows a typical AFM scan of the α -Ga₂O₃ surface, dominated by triangular features representative of the symmetry of the α crystal phase.

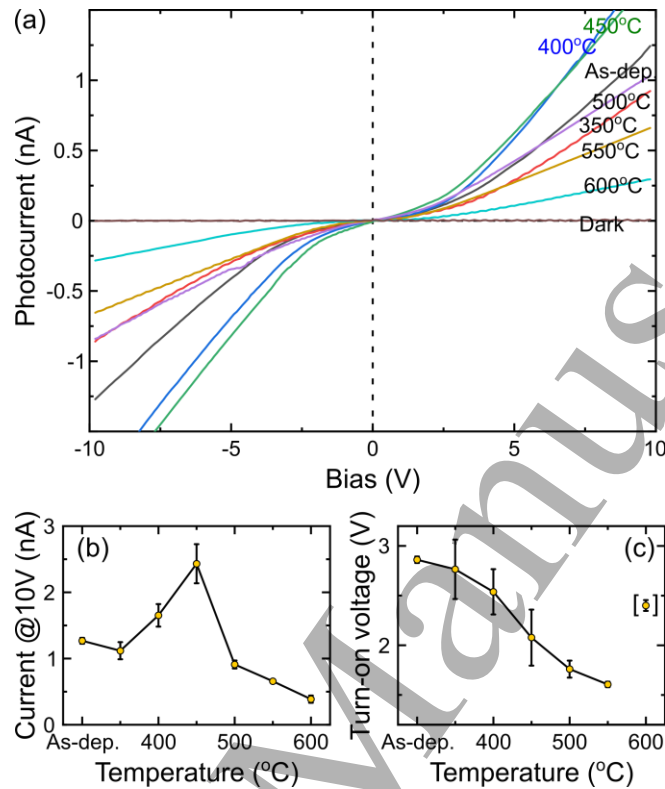


Fig. 2. (a) Photo I-V characteristics, (b) photocurrent at 10 V, and (c) turn-on voltage of the samples annealed at different temperatures.

The electrical behaviour of the contacts was measured. Since the films were nominally undoped and hence too resistive, the I-V characteristics were obtained under 240 nm light illumination to increase their conductivity. Liu *et al.* showed that the ohmic or rectifying nature of the contact was not affected by light illumination.¹³⁾ Figure 2(a) shows the photocurrent versus voltage curve for all the samples, alongside the typical dark I-V characteristic. The dark current is limited by the noise of the system, but we can already clearly see that the samples are acting as solar-blind detectors, as the photocurrent under 240 nm illumination and 10 V bias is 2-3 orders of magnitudes greater than the dark current at the same voltage.

The main observation from Figure 2(a) is that all the I-V curves show that Ni/Au forms a rectifying contact to α -Ga₂O₃, irrespective of the post-deposition annealing conditions. This is in line with previous reports on β -Ga₂O₃.^{13, 15, 18, 23, 24)} This finding can be partially

rationalised by the fact that the electron affinity of (0001)-oriented α -Ga₂O₃ has been calculated at 3.62 eV,³⁶⁾ while the workfunctions of (111)-oriented Ni and Au are 5.24 eV and 5.33 eV, respectively.³⁷⁾

Besides the rectifying behaviour common for all the contact structures, we observe variations in photocurrent at 10 V (Figure 2(b)) and turn-on voltage (Figure 2(c)). Figure 2(b) shows that the photocurrent increases about two-fold when the structure is annealed at 400-450°C, then rapidly decreases if the anneal is conducted at greater temperatures. In terms of turn-on voltage in Figure 2(c), we observe that the turn-on voltage (note that this is under illumination) is relatively stable at low annealing temperatures, then gradually decreases over the *ca.* 400-500°C range, then stabilises again for greater annealing temperatures (note that the datapoint at 600°C could not be reliably determined due to the noisy signal and shallow increase of the I-V curve for this sample).

Collating our observations from Figures 1(a) and 2(b-c) allow us to distinguish 3 main regimes: (i) A first regime seen when there is no anneal or the annealing temperature is low ($\leq 350^\circ\text{C}$) where the structure is close to as-deposited; (ii) a second regime of medium (400-450°C) annealing conditions where the Au and Ni just start interdiffusing, the photocurrent is maximal, and the turn on voltage decreases; and finally (iii) a third regime of harsher annealing conditions ($\geq 500^\circ\text{C}$) where Au-Ni alloying is significantly more pronounced, and where the photocurrent is degraded. From Figure 2(b), medium annealing conditions are favourable to the electric performance of the contact structure.

Figure 3 presents HAADF-STEM images and elemental maps extracted from EDX measurements of samples corresponding to the 3 regimes highlighted above.

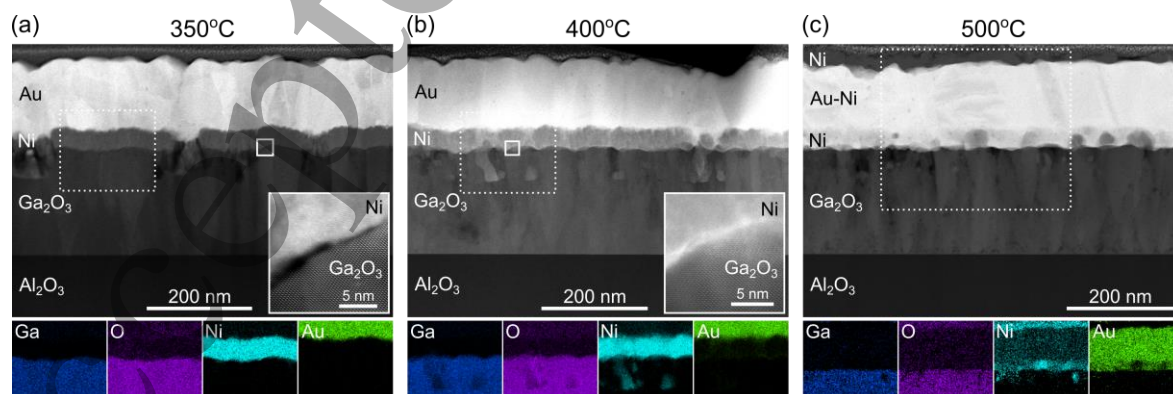


Fig. 3. TEM images and EDX maps of the samples annealed at (a) 350°C, (b) 400°C, and (c) 500°C.

1
2
3
4
5
6
7
8
9
10
11
12
13
14
15
16
17
18
19
20
21
22
23
24
25
26
27
28
29
30
31
32
33
34
35
36
37
38
39
40
41
42
43
44
45
46
47
48
49
50
51
52
53
54
55
56
57
58
59
60

Figure 3(a) shows the contact structure annealed at 350°C, that is, where the anneal temperature is too low to induce significant changes. The image shows that the sample and contact structure is as expected from the deposition procedure. The α -Ga₂O₃ film consists of triangular columns of high crystalline quality which thread up to the top surface of the film (as shown by the high resolution image in inset) with amorphous material between the columns (slightly darker contrast in the film), in line with previous cross sectional images of PEALD Ga₂O₃ samples.^{22, 29, 30)} In places, we observe a significant gap between α -phase columns, where the top surface of the film lies *ca.* 60 nm below the rest of the film. This was observed in other films where Ti contacts were deposited,²²⁾ but not on films without contacts.^{30, 34)} In our previous work we noticed that the developer solution containing tetramethylammonium hydroxide (TMAH) used during contact deposition could etch the film,³⁴⁾ hence minimal exposure was used. More recent reports have found that TMAH etched amorphous Ga₂O₃,³⁸⁾ but not β -Ga₂O₃.³⁹⁾ We therefore attribute these features to the preferential etching of amorphous Ga₂O₃ by the TMAH. Analysis of the Ga₂O₃/Ni interface region, in inset of Figure 3(a), reveals that the Ni layer is polycrystalline, and while it is directly deposited on top of the α -Ga₂O₃ film, we note the presence of a number of nanometer-thick gaps between the α -Ga₂O₃ and Ni. These gaps certainly originate from the deposition process of Ni on the semiconductor. The Au layer is also polycrystalline, but forms already large grains as could be expected from the Au reflection seen by XRD in Figure 1(a). Looking at the interface region by EDX, we can see that all the layers are chemically distinct, with no sign of diffusion between the layers.

40
41
42
43
44
45
46
47
48
49
50
51
52
53
54
55
56
57
58
59
60

Figure 3(b) shows the structure annealed at 400°C, that is, the structure at the onset of which Ni-Au alloy becomes noticeable by XRD, and also the structure that exhibits best electrical properties alongside that annealed at 450°C. The structure is very similar to that shown in Figure 3(a), and the major difference to be noted is that the interface between the crystalline α -Ga₂O₃ and Ni films no longer contains gaps (see inset). We also observe that the Ni film starts appearing more granular, and EDX analysis shows that Au is present at the Ni grain boundaries. We note that the α -Ga₂O₃/Ni interface looks rougher, which is difficult to interpret with certainty. This is probably due to a projection effect in TEM as the columns are of similar dimensions as the thickness of the TEM lamella. The faint presence of Au at the interface, however, makes it difficult to draw conclusive interpretations of the contrast at the interface. We rule out surface reconstruction effects at this temperature, as our AFM data show no difference of topography upon annealing. Lastly, in the troughs formed by selective etching of amorphous Ga₂O₃ by TMAH, Ni is still present in its metallic form –

probably formed by the wetting of the Ni that was initially sputtered inside these throughs. It appears more encapsulated within the Ga_2O_3 matrix; however we cannot draw firm conclusions as these Ni inclusions are of small dimensions and this could be a projection effect from the TEM. This image overall shows that this annealing condition is the onset of metal atoms diffusion, which main effect here is to “heal” the gaps at the interface with the Ga_2O_3 and likely the reason for the improved electrical performances.

Figure 3(c) presents the cross-sectional analysis of the sample annealed at 500°C , that is, the regime where XRD detected significant mixing between Au and Ni, and the photocurrent was significantly lower. As in Figure 3(a-b), we observed the presence of Ni in the troughs formed by selective etching of amorphous Ga_2O_3 by TMAH. As above, these Ni-containing precipitates (their exact chemical nature cannot be conclusively ascertained due to projection effects in the TEM) probably originate from the initial sputtering of Ni inside the troughs. The most noticeable feature in this image is the significant interdiffusion between Au and Ni. The Ni/Au structure can now be described as a 3-layer structure. Starting from the bottom, what used to be a uniform Ni layer is now a layer containing roughly spherical Ni-rich precipitates (*ca.* 91% Ni) within a Au-Ni solid solution (*ca.* 46% Ni). Above that layer, we find a Au-Ni alloy layer of slightly lower Ni fraction (*ca.* 17% Ni). Finally a top-most layer of NiO_x has formed. Outdiffusion of Ni to the surface of Ni/Au contacts have also been reported in literature for GaN contacts annealed at similar temperatures in oxidising atmospheres.^{26, 27)} Here, since the anneal was conducted under N_2 ambient, we estimate that the top-most NiO_x layer oxidised when the sample was exposed to air after the anneal. In this structure, the Ga_2O_3 film is therefore in contact with a Ni-Au alloy layer with very variable Ni fraction, resulting in highly non-uniform Schottky barrier heights across the contact area.

An interesting observation to be made is that – in comparison to Ti contacts to α - and β - Ga_2O_3 annealed at the same temperatures^{19, 22)} – no redox reaction has occurred between the semiconductors and the metal, which concurs with findings for Ni on β - Ga_2O_3 .²⁰⁾ This is not surprising as the Gibbs free energy for the Ni/NiO couple is greater than that of Ga/(β -) Ga_2O_3 at all temperatures and partial pressures of O_2 , meaning that oxidation of the Ni metal contact by Ga_2O_3 is not expected at any annealing temperature.

4. Conclusions

We have investigated the structural, chemical and electrical properties of Ni contacts to α -Ga₂O₃ and linked the electrical performance to the chemical and metallurgical processes at play during metal contact thermal treatment. Ni forms a Schottky contact with α -Ga₂O₃, irrespectively of the post-annealing temperature. No sign of metal oxidation was observed at the metal-semiconductor interface (unlike with other metals like Ti). Instead, we find that the metallurgical processes of the Ni-Au bilayer dominate the impact on the electrical properties. For low ($T \leq 350^\circ\text{C}$) temperature anneal, the contact is negatively affected by small gaps present at the metal/semiconductor interface stemming from the metal deposition. For medium ($400^\circ\text{C} \leq T \leq 450^\circ\text{C}$) anneal, metal diffusion starts becoming thermally activated, allowing to heal the interface gaps, but is not sufficient for significant Au-Ni interdiffusion to occur. For greater ($T \leq 500^\circ\text{C}$) anneals, the increase in metal diffusion provokes significant Au-Ni interdiffusion leading to highly non-uniform interface properties across the contact area.

Acknowledgments

The authors acknowledge support from the Royal Society (RGS/R1/201236), the Engineering and Physical Sciences Research Council (EP/T517938/1; EP/P00945X/1; EP/M010589/1; EP/K014471/1), and the European Union's Horizon 2020 research and innovation programme (grant agreement No 823717-ESTEEM3). The data that support the findings of this study are openly available in PurePortal at [INSERT LINK].

References

- 1) S.J. Pearton, J. Yang, P. Cary, F. Ren, J. Kim, M. Tadjer, and M. Mastro, *Appl. Phys. Rev.* **5**, 011301 (2018).
- 2) D. Kaur, and M. Kumar, *Adv. Opt. Mater.* **9**, 2002160 (2021).
- 3) A. Green, J. Speck, G. Xing, P. Moens, F. Allerstam, K. Gumaelius, T. Neyer, A. Arias-Purdue, V. Mehrotra, A. Kuramata, K. Sasaki, S. Watanabe, K. Koshi, J. Blevins, O. Bierwagen, S. Krishnamoorthy, K. Leedy, A. Arehart, A. Neal, S. Mou, S. Ringel, A. Kumar, A. Sharma, K. Ghosh, U. Singiseti, W. Li, K. Chabak, K. Liddy, A. Islam, S. Rajan, S. Graham, S. Choi, Z. Cheng, and M. Higashiwaki, *APL Mater.* **10**, 029201 (2022).
- 4) R. Roy, V. Hill, and E. Osborn, *J. A. Chem. Soc.* **74**, 719 (1952).
- 5) H. Playford, A. Hannon, E. Barney, and R. Walton, *Chem. – A European Journal* **19**, 2803 (2013).
- 6) I. Cora, F. Mezzadri, F. Boschi, M. Bosi, M. Caplovicova, G. Calestani, I. Dodony, B. Pecz, and R. Fornari, *CryslEngComm* **19**, 1509 (2017).
- 7) S. Fujita, and K. Kaneko, *J. Cryst. Growth* **401**, 588 (2014).
- 8) J. Jinno, C. Chang, T. Onuma, Y. Cho, S.T. Ho, D. Rowe, M. Cao, K. Lee, V. Protasenko, D. Schlom, D. Muller, H. Xing, and D. Jena, *Sci. Advances* **7**, eabd5891 (2021).
- 9) A. Barthel, J. Roberts, M. Napari, M. Frentrup, T. Huq, A. Kovacs, R. Oliver, P. Chalker, T. Sajavaara, and F. Massabuau *Micromachines* **11**, 1128 (2020).
- 10) K. Kaneko, K. Uno, R. Jinno, and S. Fujita, *J. Appl. Phys.* **131**, 090902 (2022).
- 11) D. Yang, B. Kim, T. Eom, Y. Park, and H. Jang, *Elec. Mater. Lett.* **18**, 113 (2022).
- 12) C. Xie, X.T. Lu, X.W. Tong, Z.X. Zhang, F.X. Liang, L. Liang, L.B. Luo, and Y.C. Wu, *Adv. Func. Mater.* **29**, 1806006 (2019).
- 13) Z. Liu, Y. Zhi, S. Li, Y. Liu, X. Tang, Z. Yan, P. Li, X. Li, D. Guo, Z. Wu, and W. Tang *J. Phys. D: Appl. Phys.* **53**, 085105 (2020).
- 14) H. Kim, *SN Appl. Sci.* **4**, 27 (2022).
- 15) L. Porter, and J. Hajzus, *J. Vac. Sci. & Tech. A* **38**, 031005 (2020).
- 16) M.H. Lee, and R. Peterson, *J. Mater. Res.* **36**, 4771 (2021).
- 17) Y. Yao, R. Davis, and L. Porter, *J. Elec. Mater.* **46**, 2053 (2017).
- 18) L. Lyle, K. Jiang, E. Favela, K. Das, A. Popp, Z. Galazka, G. Wagner, and L. Porter, *J. Vac. Sci. & Tech. A* **39**, 033202 (2021).

- 19) M.H. Lee, and R. Peterson, *APL Mater.* **7**, 022524 (2019).
- 20) H. Aller, X. Yu, A. Wise, R. Howell, A. McGaughey, and J. Malen, *Nano Lett.* **19**, 8533 (2019).
- 21) L. Lyle, T. Back, C. Bowers, A. Green, K. Chabak, D. Dorsey, E. Heller, and L. Porter, *APL Mater.* **9**, 061104 (2021).
- 22) F. Massabuau, D. Nicol, F. Adams, J. Jarman, J. Roberts, A. Kovacs, P. Chalker, and R. Oliver, *J. Phys. D: Appl. Phys.* **54**, 384001 (2021).
- 23) E. Farzana, Z. Zhang, P. Paul, A. Arehart, and S. Ringe, *Appl. Phys. Lett.* **110**, 202102 (2017).
- 24) H. Kim, S. Kyoung, T. Kang, J.Y. Kwon, K. Kim, and Y. Rim, *J. Mater. Chem. C* **7**, 10953 (2019).
- 25) J. Sheu, Y. Su, G. Chi, W. Chen, C. Chen, J. Hong, Y. Yu, C. Wang, and E. Lin, *J. Appl. Phys.* **83**, 3172 (1998).
- 26) J. Smalc-Koziorowska, S. Grzanka, E. Litwin-Staszewska, R. Piotrkowski, G. Nowak, M. Leszczynski, P. Perlin, E. Talik, J. Kozubowski, and S. Krukowski, *Solid-State Elec.* **54**, 701 (2010).
- 27) L.C. Chen, F.R. Chen, J.J. Kai, L. Chang, J.K. Ho, C.S. Jong, C. Chiu, C.N. Huang, C.Y. Chan, and K.K. Shih, *J. Appl. Phys.* **86**, 3826 (1999).
- 28) A. Herz, D. Wang, T. Kups, and P. Schaaf, *J. Appl. Phys.* **116**, 044307 (2014).
- 29) F. C-P. Massabuau, J. Roberts, D. Nicol, P. Edwards, M. McLelland, G. Dallas, D. Hunter, E. Nicolson, J. Jarman, A. Kovacs, R. Martin, R. Oliver, and P. Chalker, *Proc. SPIE* **11687**, 116870Q (2021).
- 30) J. Roberts, J. Jarman, D. Johnstone, P. Midgley, P. Chalker, R. Oliver, and F.C-P. Massabuau, *J. Cryst. Growth* **487**, 23 (2018).
- 31) J. Swallow, C. Vorwerk, P. Mazzolini, P. Vogt, O. Bierwagen, A. Karg, M. Eickho, J. Schormann, M. Wagner, J. Roberts, P. Chalker, M. Smiles, P. Murgatroyd, S. Razek, Z. Lebens-Higgins, L. Piper, L. Jones, P. Thakur, T.L. Lee, J. Varley, J. Furthmuller, C. Draxl, T. Veal, and A. Regoutz, *Chem. Mater.* **32**, 8460 (2020).
- 32) A. Kovacs, R. Schierholz, and K. Tillmann, *Journal of large-scale research facilities* **2**, A43 (2016).
- 33) G. Cliff, and G. Lorimer, *J. Micro.* **103**, 203 (1975)
- 34) J. Moloney, O. Tesh, M. Singh, J. Roberts, J. Jarman, L. Lee, T. Huq, J. Brister, S. Karboyan, M. Kuball, P. Chalker, R. Oliver, and F.C-P. Massabuau, *J. Phys. D: Appl. Phys.* **52**, 475101

1
2
3 (2019).
4

5 35) A. Crawley, and D. Fabian, J. Institute Metals **94**, 39 (1966).
6

7 36) Y. Hinuma, T. Gake, and F. Oba, Phys. Rev. Mat. **3**, 084605 (2019).
8

9 37) G. Derry, M. Kern, and E. Worth, J. Vac. Sci. & Tech. A **33**, 060801 (2015).
10

11 38) Z. Han, H. Liang, W. Huo, X. Zhu, X. Du, and Z. Mei, Adv. Opt. Mater. **8**, 1901833 (2020).
12

13 39) H. Okumura, and T. Tanaka, Jap. J. Appl. Phys. **58**, 120902 (2019).
14
15
16
17
18
19
20
21
22
23
24
25
26
27
28
29
30
31
32
33
34
35
36
37
38
39
40
41
42
43
44
45
46
47
48
49
50
51
52
53
54
55
56
57

58 **Figure Captions**

59 **Fig. 1.** (a) Symmetric 2θ - ω XRD scans of the samples annealed at different
60

1
2
3
4
5
6
7 temperatures. (b) Redrawn phase diagram for Au-Ni. (c) AFM topography image
8 of the α -Ga₂O₃ surface.
9

10
11
12 **Fig. 2.** (a) Photo I-V characteristics, (b) photocurrent at 10 V, and (c) turn-on voltage of the
13 samples annealed at different temperatures.
14
15

16
17 **Fig. 3.** TEM images and EDX maps of the samples annealed at (a) 350°C, (b)
18 400°C, and (c) 500°C.
19
20
21
22
23
24
25
26
27
28
29
30
31
32
33
34
35
36
37
38
39
40
41
42
43
44
45
46
47
48
49
50
51
52
53
54
55
56
57
58
59
60

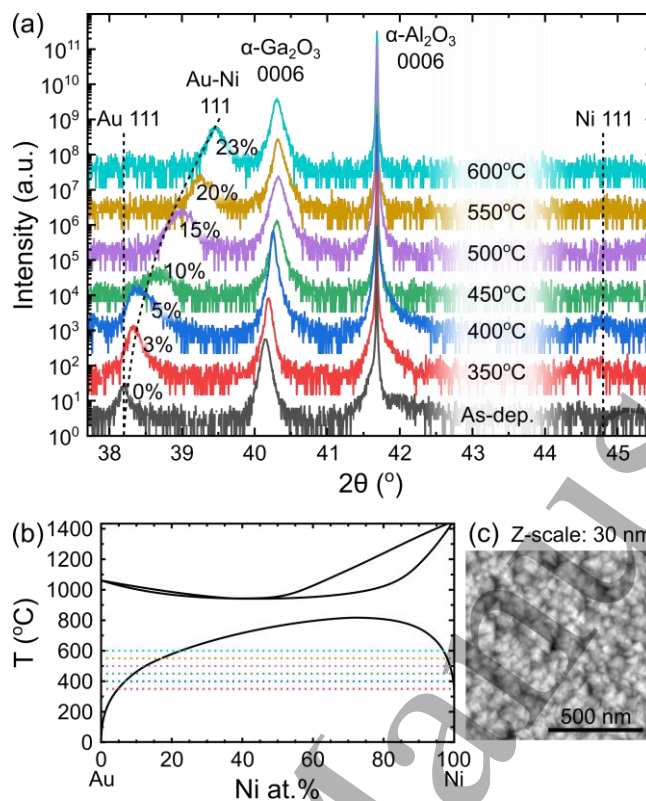


Fig. 1. (a) Symmetric 2θ - ω XRD scans of the samples annealed at different temperatures. (b) Redrawn phase diagram for Au-Ni. (c) AFM topography image of the α -Ga₂O₃ surface.

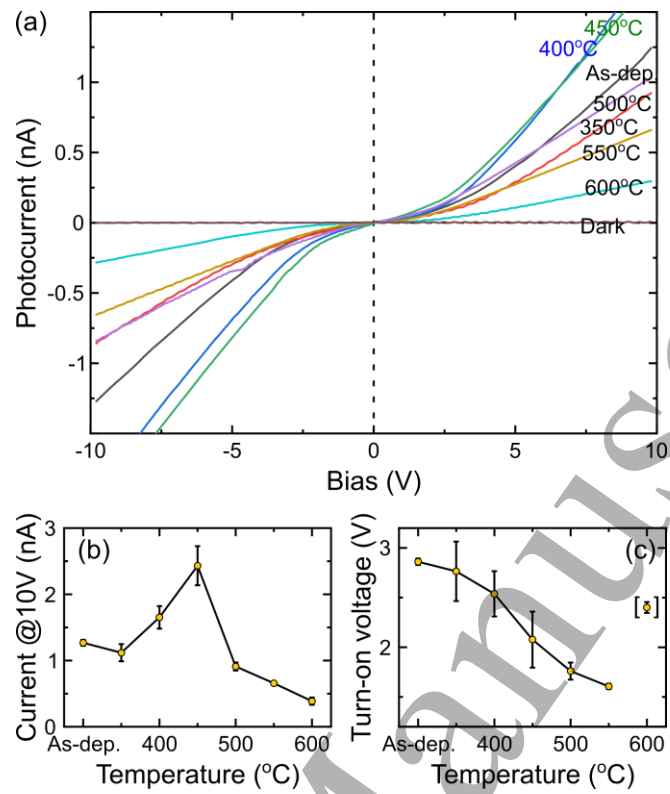


Fig. 2. (a) Photo I-V characteristics, (b) photocurrent at 10 V, and (c) turn-on voltage of the samples annealed at different temperatures.

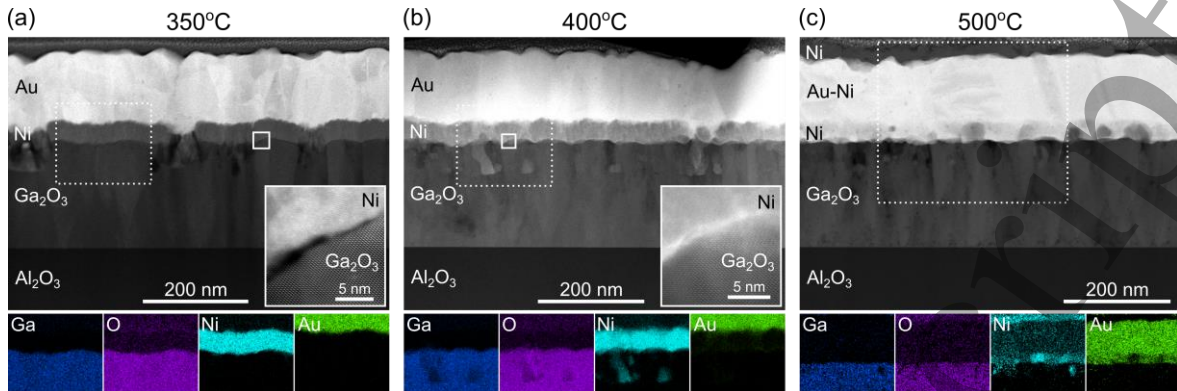


Fig. 3. TEM images and EDX maps of the samples annealed at (a) 350°C, (b) 400°C, and (c) 500°C.